Glass#Ceramic#Like Vanadate Cathodes for High#Rate Lithium#Ion Batteries

DOI: 10.1002/aenm.201903411

Article type: Communication

Glass-ceramic-like vanadate cathodes for high-rate lithium-ion batteries

Yutong Li, Shitong Wang, Yanhao Dong*, Yong Yang, Zhongtai Zhang and Zilong Tang**

Ms. Y. Li, Prof. Z. Zhang, Prof. Z. Tang

State Key Laboratory of New Ceramics and Fine Processing, School of Materials Science and Engineering, Tsinghua University, Beijing 100084, P. R. China

Email: tzl@mail.tsinghua.edu.cn

Dr. S. Wang, Dr. Y. Dong

Department of Nuclear Science and Engineering, Massachusetts Institute of Technology, Cambridge, Massachusetts 02139, USA

Email: wangst@mit.edu; dongyh@mit.edu

Dr. Y. Yang

Department of Materials Science and Engineering, College of Engineering, Peking University, Beijing 100871, P. R. China

Keywords: Microstructures, kinetics, batteries, cathodes, vanadate

Abstract

Nanostructured electrode materials are good candidates in batteries especially for high-rate applications, yet they often suffer from extensive side reactions due to anomalously large surface areas. On the other hand, while micron-size materials provide better stability, the lattice diffusivity is often too slow for lithium ion intercalation over the same length scale in a short time. Herein, we report a simple method to synthesize glass-ceramic-like vanadate cathodes for lithium-ion batteries with abundant internal boundaries that allow fast lithium ion diffusion yet a small surface area that minimizes contact and side reactions with organic electrolyte. Such samples heat-treated under optimized conditions can deliver an impressive high-rate capacity of 103 mAh g^{-1} at 4000 mA g^{-1} over 500 cycles, which has better kinetics and cycling stability than similar vanadate-based materials. We also found a striking grain-size refinement effect accompanied by a low-temperature growth-controlled phase transition, which can be achieved by a fine tuning of the heat-treatment process. We believe our findings are general for other transition metal oxides for energy applications, and there is plenty of room at the interfaces and in processing as simple as heat treatment.

Nanomaterials have brought much advances in energy technology[1]. For applications in lithium-ion batteries (LIBs), nano electrode materials are good because they offer short diffusion distance, fast kinetics and peculiar surface effects including pseudocapacitive charge storage and different reaction mechanisms. However, due to anomalously large surface areas, they often suffer from extensive side reactions with organic electrolytes under *operando* conditions and are prone to jamming and agglomerations during electrode preparation and battery cycling, which result in low volumetric energy density, low coulombic efficiency and fast degradation[2]. Therefore, the

integration of nanomaterials into stable micro-/macro-sized hierarchical structures are of equal importance to their synthesis. From this perspective, micron-scale dense nanocrystalline materials with abundant two-dimensional grain boundaries or hetero-interfaces provide many opportunities, since electronic/ionic conduction can still proceed via short-circuit diffusion pathway, while direct contact between active materials and electrolytes is minimized which can greatly suppress side reactions[3]. Approximately, one may view such material as a partially closed system that hardly exchange its chemical constitutions with the environment (i.e. organic electrolytes), in contrast with the very open system of un-assembled nanoparticles.

The common way to achieve the above is to form secondary particles via bottom-up assembly (so-called granulation)[4]. Practical examples include self-agglomeration during co-precipitation of layered cathodes $LiNi_{1-x-y}Co_xMn_yO_2$ and $LiNi_{0.8}Co_{0.15}Al_{0.05}O_2$[5], and spray drying of olivine-type cathode $LiFePO_4$[6], both of which have achieved great commercial success. Nevertheless, there are alternative top-down methods, which are extremely simple and not well recognized. These are like crystallization of glass[7], or recrystallization of metals under plastic formation and phase transitions[8]. In ceramics, the latter is also known to be assisted by the evolution of gaseous species, e.g. during the thermal decomposition of $CaCO_3$ to CaO[9]. Similar concepts also lead to the invention of glass-ceramics, where the unique combination of nano-grained crystalline precipitates and a dense amorphous matrix provides many interesting properties and various applications[10]. Such controlled (re-)crystallization and phase transition processes naturally apply to the synthesis of battery electrodes, since many of them are derived from poorly crystallized hydrates and go through a series of phase transitions before the end products are obtained. It is the aim of the present study to demonstrate that this approach provides simultaneously improved kinetics and stability by a simple one-step heat-treatment of the precursor, in a model system of vanadate cathodes.

Vanadium oxides and their derivatives are interesting cathodes for LIBs, because the rich chemistry of V enables multi-electron redox per transition metal (hence a high capacity), the open structure (often layered one) formed by V-O polyhedra allows for fast Li^+ intercalation, and the numerous polymorphs provide much room to tune the atomic structures and electrochemical properties[11]. They have been attracting continuous research interests since the initial explorations of their applications in LIBs in 1970s and has enjoyed another boost since 2013 in not only LIBs but also other emerging systems such as Na^+, Mg^{2+} and Al^{3+} batteries[3b, 3c, 12]. Previous studies are mostly on high-temperature (>350 °C) treated vanadium oxide/vanadate[13], amorphous-like bilayer $V_2O_5{\cdot}nH_2O$ dried at low temperatures (<250 °C)[14] and ammonium vanadium bronze $NH_4V_4O_{10}$ obtained at low temperatures (<180 °C)[15]. Little attention has been paid at the intermedium temperature regime (~200-350 °C), where partial decomposition of hydrate precursors may give rise to a nanocrystalline two-phase mixture with some residue "water" within the structure. As shown by our recent work in lithium titanate hydrates[16], such "water" residues in the form of -H or -OH may not necessarily degrade the H_2O-senstive battery electrolytes, as long as the loosely bounded water is removed at 100-150 °C. Furthermore, the intermedium temperatures are low enough to suppress the kinetics of nanostructure coarsening, while partial decomposition of precursors may even refine the grain size as will be shown later. To the end, we show nanocrystalline vanadate cathodes heat-treated under optimized conditions can deliver an impressive high-rate capacity, 103 mAh g^{-1} at 4000 mA g^{-1} over 500 cycles, which has much better kinetics and cycling stability than the ones reported in the literature.

Vanadate cathodes investigated in this work were synthesized by a two-step hydrothermal method and then heat-treated at various temperatures (**Figure 1a**). Ammonium metavanadate (NH_4VO_3) and oxalic acid ($H_2C_2O_4$) were first hydrothermally treated in aqueous solution at 160 °C for

12 h, then followed by a second-step hydrothermal treatment at 180 °C for 12 h with lithium hydroxide (LiOH). Thus-obtained precursor (denoted as V-P hereafter) contains a large amount of loosely bounded water and the kinetics of dehydration was investigated by thermogravimetric analyzer (TGA) in **Figure 1b**. Upon heating, rapid weight loss first occurs below ~120 °C, due to the removal of physically absorbed water. A plateau follows with little weight loss up to ~250 °C, beyond which continuous weight loss takes place up to 600 °C, indicating the removal of structurally bonded -OH and/or -NH_4 groups. Such a gradual weight loss suggests versatilely bonded H_2O/-OH/-NH_4 inside the materials, which may be utilized to fine-tune the chemistry, atomic structure and electrochemical properties. This fine tuning is the focus of the present study and three samples with different levels of dehydration were of particular interests: (i) heat-treated at 80 °C for 2 h, denoted as V-80 hereafter; (ii) heat-treated at 270 °C for 2 h, denoted as V-270 hereafter; and (iii) heat-treated at 450 °C for 2 h, denoted as V-450 hereafter. From the data of elemental analyzer measurements and inductively coupled plasma mass spectroscopy (ICP-MS), their chemical compositions were estimated to be $Li_{0.01}(NH_4)_{0.46}V_2O_{4.77}{\cdot}0.28H_2O$ for V-80, $Li_{0.01}(NH_4)_{0.23}V_2O_{4.77}(OH)_{0.56}$ for V-270, and $Li_{0.01}V_2O_{4.79}(OH)_{0.33}$ for V-450. Fourier-transform infrared spectroscopy (FTIR) results in **Figure 1c** found the vibrations of (i) V-OH groups (so-called bridging hydroxyl)[14e] around 3400 cm^{-1} for all three samples, confirming the existence of H-containing groups even after 450 °C heat-treatment; (ii) surface H_2O around 3200 cm^{-1}[14e] for V-80 but not for V-270 and V-450, indicating rapid removal of physically absorbed (surface) water below 270 °C; (iii) -NH_4 groups around 1400 cm^{-1}[17] for V-80 and V-270 but not for V-450, indicating removal of -NH_4 above 270 °C; (iv) V-O-V groups around 800 cm^{-1} and V=O groups at 1000 cm^{-1}[18] for all three samples, where both peaks red-shift from V-80 to V-270 to V-450 indicating shorter V-O bond length and stronger bond strength probably in higher temperature treated samples due to oxidation of vanadium. Lastly, X-ray

photoelectron spectroscopy (XPS) measurements in **Figure 1d** show existence of both V^{5+} and V^{4+}[19] in V-80, but a diminishing population of V^{4+} (correspondingly an increasing population of V^{5+}) in V-270 and V-450, which agrees with FTIR data (iv). Therefore, there is gradual vanadium oxidation accompanied by water removal during heat-treatment.

Along with the evolving chemistry upon heating, the materials also go through a series of phase transitions. As shown by *in situ* X-ray diffraction (XRD, **Figure 2a**), the structure transforms from a low-temperature $NH_4V_4O_{10}$-like phase (denoted as *α* phase hereafter; similar to JCPDF 31-0075) first to an intermedium-temperature phase (denoted as *β* phase hereafter) around 270 °C, then to a high-temperature V_2O_5-like or $Li_xV_2O_5$-like phase (denoted as *γ* phase hereafter; similar to JCPDF 72-0433 or JCPDF 85-0608) above 350 °C (**Figure S1** in Supporting Information). The phase transitions are most vividly shown by the contour plot of low-angle diffraction patterns (2ϑ from 8^o to 11^o) in **Figure 2b**, where *α* and *β* phases with large *d*-spacing co-exist at 270-300 °C and they all transform to *γ* phase above 350 °C. Interestingly, associated with the phase transitions, there are apparent variations in the XRD peak broadening, which could arise from changes in either crystalline domain size or lattice distortion (defects). While the two effects cannot be well separated for defect-rich materials, for better quantification, we used the Scherrer equation to estimate the grain/crystalline domain size that is responsible for the broadening (i.e. assuming peak broadening solely comes from the size effect). As shown in **Figure 2c**, it provides a striking grain-size refinement effect that coincides with the onset of the *α*→*β* transition: In contrast with gradually coarsened grain size of *α* phase (in blue) from ~20 nm to ~35 nm below 250 °C, it decreases to ~13 nm at 260-270 °C before completely transformed to *β* phase. Meanwhile, the precipitating *β* phase has extremely fine grain size of ~11 nm at 270 °C, which gradually coarsens with further grain size increasement during annealing. Such a refinement does not apply for *β*→*γ* transition at 330-350 °C, during which the

grain sizes of both *β* and *γ* phases remain ~35 nm without apparent changes. These observations suggest that (i) *α*→*β* transition around 260-270 °C is probably growth controlled, where one or more *β* nuclei first precipitate inside an *α* grain and gradually grow at the expense of shrinking *α* phase; and (ii) *β*→*γ* transition around 330-350 °C is probably nucleation controlled, where a *β* grain completely transforms to *γ* phase immediately after the nucleation stage, which explains why *α*→*β* transition can refine the grain size while *β*→*γ* cannot.

The microstructures of optimized *ex situ* synthesized samples were next investigated under scanning electron microscope (SEM) and transmission electron microscope (TEM). A key feature is that all the samples (V-80 in **Figure 2d**, 260 °C treated sample V-260 in **Figure 2e-g**, V-270 in **Figure 2h-j**, V-450 in **Figure 2k**; here the numbers refer to the furnace temperatures during *ex situ* heat-treatment) have similar plate-like morphology with approximately 1 μm length, 200 nm width and 20 nm thickness (**Figure S2** in Supporting Information). Their surface areas are in the range of 10-20 m^2 g^{-1} according to Brunauer-Emmett-Teller (BET) measurements (**Figure S3** & **Table S1** in Supporting Information), which are smaller than typical nanomaterials reported in the literature[20] and are expected to minimize side reactions with organic electrolytes during battery cycling. For V-260 and V-270, we found the sub-micron plates are two-phase composites, consisted of fine *α* and *β* phases with a few nanometer size as confirmed by high-resolution TEM (V-260 in **Figure 2f** and V-270 in **Figure 2i**; more examples shown in **Figure S4** in Supporting Information) and selected area diffraction (inset of **Figure 2f** and **2i**). Here, for *α* phase, characteristic spacings of 0.96 nm for (001) plane (corresponding to 2ϑ=9.2° in XRD) and 0.35 nm for (110) plane (corresponding to 2ϑ=25.5°) are marked in blue; for *β* phase, characteristic spacings of 0.85 nm (corresponding to 2ϑ=10.3°) and 0.57 nm (corresponding to 2ϑ=15.5°), and 0.42 nm (corresponding to 2ϑ=21.0°) are marked in green (their XRD data are plotted in **Figure S5** in Supporting Information). Meanwhile, abundant

amorphous-like (glass) structures are noted in HRTEM of **Figure 2g** and **2j** (circled in yellow). Besides, the protons in disordered surface layer can also be detected in ^{1}H MAS-NMR spectrum (**Figure S6** in Supporting Information). Therefore, dense glass-ceramic-like composites with nanocrystalline α and β phases have been successfully synthesized (**Figure 2l**), whose electrochemical properties shall be studied in the following.

The electrochemical properties of the synthesized vanadate cathodes are tested in half cells using lithium metal as the counter and reference electrode. Cyclic voltammetry (CV) curves in **Figure 3a** show that V-80 (α phase in blue) and V-270 (α-β phase mixture in red) have similar redox behaviors with multiple redox peaks, while V-450 (γ phase in black) has a more diffusive curve without any obvious peaks. Their discharge capacities under various rates are plotted in **Figure 3b**. While V-270 and V-450 have similar capacity (~280 mAh g^{-1}) at 50 mA g^{-1}, V-270 has much better capacity retention under larger discharge currents. More specifically, V-270 shows greater discharge abilities of 175.5 mAh g^{-1} at 1000 mA g^{-1}, 155.6 mAh g^{-1} at 2000 mA g^{-1} and 135.8 mAh g^{-1} at 4000 mA g^{-1}, compared to 116.2 mAh g^{-1} at 1000 mA g^{-1}, 62.7 mAh g^{-1} at 2000 mA g^{-1} and 25.4 mAh g^{-1} at 4000 mA g^{-1} for V-450. In comparison, V-80 has much lower capacity of ~190 mAh g^{-1} at 50 mA g^{-1} hence less useful, even though it has better rate performance than V-450. Here, we note the first cycle discharge capacity of all three samples are much higher than the following cycles. This is because the as-synthesized samples do not contain much lithium, so they require a pre-lithiation step (i.e. first discharge) before following charge/discharge cycles. The cycling of V-270 was next evaluated at 1000 mA g^{-1} (**Figure 3c**; data of V-80 and V-450 are also plotted for comparison) and 4000 mA g^{-1} (**Figure 3d**; coulombic efficiency is plotted as right y-axis), both of which show good stability. Specifically, after 500 cycles at 4000 mA g^{-1}, V-270 has a capacity of 103.3 mAh g^{-1} with nearly 100% coulombic efficiency, corresponding to 0.037% capacity loss per cycle. Consistent with

the electrochemical stability, we also confirmed the plate-like morphology (**Figure S7a** in Supporting Information), glass-ceramic-like structure (**Figure S7b-c** in Supporting Information), and layered structure (**Figure S7d** in Supporting Information) unchanged. Lastly, we compared the capacity of V-270 with the literature reports of vanadate related systems under different rates in **Figure 3e**[14a, 15b, 21] and **Table S2**, Supporting Information, which highlights its superior performance especially at large rates of >2000 mA g^{-1}.

The above electrochemical data indicate the improved kinetics of V-270 (sub-micron plates with 13 nm *α* phase and 11 nm *β* phase) over that of high-temperature treated V-450 (sub-micron plates with 77 nm *γ* phase) and many vanadate nanostructures reported in the literature, which is the theme of the present work—abundant internal interfaces/grain boundaries provide numerous Li^+ diffusion pathways. We next quantified the kinetics by diffusivity data obtained from electrochemical impedance spectroscopy (EIS) and galvanostatic intermittent titration technique (GITT) data. EIS measurements were conducted on cells discharged at 50 mA g^{-1} to the target voltage, which show a typical (depressed) semi-circle at high-frequency range representing the charge transfer process and a Warburg diffusion element at low-frequency range representing the diffusion process (**Figure S8** in Supporting Information). As shown in **Figure 3f** (each sample was activated for 5 cycles at 50 mA g^{-1}), the charge transfer resistance R_{ct} gradually increases from V-80 to V-270 to V-450, which follows the same trend of decreased V^{4+} population according to XPS data in **Figure 1d**. (Note the rate-limiting step for the charging/discharging is Li^+ conductivity rather than electronic conductivity, so modest increase in charge transfer resistance—less than two times from V-80 to V-270—is not detrimental to the rate performance.) Li^+ diffusivity (D_{Li}) is next calculated from Warburg element using the following equation

$$D_{\mathrm{Li}} = \frac{1}{2}\left(\frac{V_{\mathrm{m}}}{FAk}\right)^2\left(\frac{dE}{dx}\right)^2 \qquad (1)$$

where V_m is the molar volume of the active material (taken as 54 cm^3 mol^{-1} of V_2O_5 for all three samples), F is Faraday constant, A is the electrode area, k is the slope at low-frequency linear part of Z'-$\omega^{-1/2}$ curve with Z' being the real part of complex impedance at angular frequency ω, E is the voltage, and dE/dx is the slope of the coulombic titration curve (**Figure S9** in Supporting Information) with x being the amount of Li^+ inserted per crystal cell unit (x=1.36 for V-80 and x=1.97 for V-270 and V-450 calculated by discharge capacities at 50 mA g^{-1}). Such obtained D_{Li} is plotted in **Figure 3g**, which shows higher diffusivity for V-270 than for V-80 and V-450 (except over 3.0 V *vs.* Li/Li^+ where D_{Li} of V-80 is slightly higher than that of V-270). To get better understandings of the kinetics under high rates, we conducted parallel GITT measurements with a titration current of 1000 mA g^{-1} (**Figure S10** in Supporting Information) and calculated D_{Li} from the following equation:

$$D_{\mathrm{Li}} = \frac{4}{\pi}\left(\frac{V_{\mathrm{m}}}{AF}\right)^2\left[I_0\left(\frac{dE}{dx}\right)\Big/\left(\frac{dE}{d\sqrt{t}}\right)\right]^2,\ t \ll \frac{L^2}{D_{\mathrm{Li}}} \qquad (2)$$

under the limit of $t \ll L^2/D_{\mathrm{Li}}$. Here, I_0 is the applied current, L is the thickness of electrode, and t is the time during the titration step with a constant current. As shown in **Figure 3h**, V-270 has similar diffusivity with V-80, much higher than that of V-450 (except over 2.5 V *vs.* Li/Li^+ where D_{Li} of V-80 is slightly higher), which is consistent with EIS results. Note that the diffusivity varies as a function of states of charge (or equivalently voltages), so the lowest diffusivity across the entire voltage window would set a kinetic bottleneck for the charge/discharge process. According to **Figure 3h**, the lowest D_{Li} is 2.8×10^{-10} cm^2 s^{-1} at 2.3 V for V-270, which is 1.1 and 3.2 times higher than that of V-80 (2.6×10^{-10} cm^2 s^{-1} at 2.3 V) and of V-450 (8.8×10^{-11} cm^2 s^{-1} at 1.8 V). From random diffusion model,

D_{Li}×(time)~D_{Li}/(charge/discharge rate) determines the accessible diffusion length thus the amount of materials that contribute to capacity. So under large rates, V-270 is expected to have similar capacity retention (normalized by the capacity under 50 mA g^{-1}) with V-80, or with V-450 under 3.2 times higher rate. This prediction is supported by the data in **Figure 3b**—the capacity retention of V-270 is 46% (of the capacity at 50 mA g^{-1}) at 4000 mA g^{-1}, which is similar to that of 41% for V-80 at 4000 mA g^{-1} and of 42% for V-450 at 1000 mA g^{-1}. This quantitative agreement suggests it is indeed the enhanced diffusivity that gives rise to the superior rate performance of V-270 over the other two samples. Lastly, we emphasize all three samples are micro-sized plates with similar surface area, so the diffusivity improvement is not an effect of free surfaces. Furthermore, as V-80 has the largest lattice spacing that is generally believed to help Li^+ diffusion, the higher D_{Li} observed in V-270 is less likely to be attributed to improved lattice diffusivity either. The above two aspects leave the most probable explanation to the abundant interfaces, grain boundaries and amorphous structures in the design of glass-ceramic-like nanocomposites.

To summarize, we demonstrated *in situ* grain-size refinement of vanadate hydrates from low-temperature phase transitions accompanied by de-hydration process, which provides a glass-ceramic-like structure containing two-phase crystalline precipitates with ~10 nm size. This top-down approach synthesized hierarchical architecture minimizes its exposure to and side reactions with organic electrolytes in battery cycling, while offering abundant short-circuit diffusion pathways for Li^+ intercalation. Such benefits make the present work one of the best practices (in terms of capacity, rate performance and cycling stability) of vanadate cathodes in LIBs ever reported. We believe this phase-transition driven microstructural refinement is common during the heat treatment of battery electrode precursors, especially for the phase transitions that are growth controlled and have large volume change and/or gas evolution. Therefore, the simple synthesis routine presented here could

be general and applicable to many other transition metal oxide electrodes, especially those derived from hydrates and carbonates, in not only LIBs but also emerging Na^+, Mg^{2+} and Al^{3+} batteries where ion diffusivity is more problematic.

Experimental Section

Materials synthesis

All the samples were synthesized by a two-step hydrothermal method followed by fine heat-treatment. (i) First hydrothermal step: NH_4VO_3 (2.34 g, >99.0%, Sinopharm Chemical Reagent Co., Ltd) was dissolved in deionized water (60 mL) at 80 °C and cooled down to room temperature. $H_2C_2O_4$ (2.52 g, >99.5%, Sinopharm Chemical Reagent Co., Ltd) was next added to the solution and stirred for 1 h, after which the mixture was sealed into an autoclave and heated up to 160 °C for 12 h. The obtained intermediate product was washed with deionized water and dried overnight. (ii) Second hydrothermal step: intermediate product (0.6 g) was added to lithium hydroxide aqueous solution (28 mL, 0.05 M, 98%, Alfa Aesar) and stirred for 1 h. The mixture was then transferred into an autoclave and heated up to 180 °C for 12 h. Such obtained product was denoted as V-P precursor in the main text, followed by different conditional heat-treatment as described earlier. For *ex situ* heat-treatment, all the samples were heated up to the target temperature and kept for 2 h under vacuum.

Materials characterizations

TGA analysis was conducted on thermogravimetric analyzer (STA 449F3) instrument in flowing N_2 at 5 °C min^{-1} ramping rate from 50 °C to 600 °C. Chemical compositions were characterized by elemental analysis (EuroEA3000 elemental analyzer) for O, N and H, and by ICP-MS (IRIS Intrepid II

XSP) for Li. FTIR spectra were obtained by Bruker spectrometer (VERTEX 70V) at 500-4000 cm^{-1}. XPS was conducted by Thermal Fisher instrument (ESCALAB 250Xi). Nitrogen adsorption-desorption measurements were conducted on volumetric adsorption apparatus (Autosorb-iQ2-MP). *In situ* XRD was collected on Rigaku Smartlab 9 kW X-ray diffractometer with Cu Kα (λ=0.154 nm) and *ex situ* XRD was collected on Bruker D8 Advance X-ray diffractometer. SEM images were taken on ZEISS microscopy (Gemini 2) and TEM images on JEOL microscopy (JEM-2100F). ^{1}H MAS-NMR spectrum was obtained by Bruker Avance III 400 MHz, which was used to analyze proton bonding state.

Electrochemical characterizations

Active material (V-80, V-270 or V-450), carbon black (Super P) and polyvinylidene fluoride (PVDF) were mixed with a mass ratio of 70:20:10 in *N*-methyl-2-pyrrolidone (NMP) solvent. The obtained slurry was pasted onto Al foil and dried. The average loading density of active materials is 1 mg cm^{-2}. All the electrochemical measurements were conducted in half cells using lithium metal as the counter/reference electrode and 1 M $LiPF_6$ in a mixture of ethylene carbonate (EC), dimethyl carbonate (DMC), and ethyl methyl carbonate (EMC) (1:1:1 in volume) as the electrolyte. Galvanostatic charge/discharge and GITT measurements were conducted on LAND CT2001A battery analyzer between 1.5-4.0 V *vs.* Li/Li^+. GITT measurements were conducted with a titration current of 1000 mA g^{-1} and a relaxation time of 15 h on cells after 30 cycles at 1000 mA g^{-1}. CV measurements (collected on cells at 1.5-4.0 V *vs.* Li/Li^+ after five cycles at 0.1 mV s^{-1}) and EIS analysis (from 0.01 Hz to 100 kHz and with AC current amplitude of 5 mV, collected on cells after five cycles at 50 mA g^{-1}) were conducted using Zahner IM6 electrochemical workstation.

Supporting Information

Supporting Information is available from the Wiley Online Library or from the author.

Acknowledgements

This study was financially supported by the National Natural Science Foundation of China (No. 51772163 and 51472137).

Received: ((will be filled in by the editorial staff))

Revised: ((will be filled in by the editorial staff))

Published online: ((will be filled in by the editorial staff))

References

[1] a) V. Augustyn, P. Simon, B. Dunn, *Energy Environ. Sci.* **2014**, *7*, 1597; b) Q. L. Wei, F. Y. Xiong, S. S. Tan, L. Huang, E. H. Lan, B. Dunn, L. Q. Mai, *Adv. Mater.* **2017**, *29*, 1602300; c) B. Dunn, H. Kamath, J. M. Tarascon, *Science* **2011**, *334*, 928; d) H. T. Sun, L. Mei, J. F. Liang, Z. P. Zhao, C. Lee, H. L. Fei, M. N. Ding, J. Lau, M. F. Li, C. Wang, X. Xu, G. L. Hao, B. Papandrea, I. Shakir, B. Dunn, Y. Huang, X. F. Duan, *Science* **2017**, *356*, 599; e) L. Qie, W. M. Chen, Z. H. Wang, Q. G. Shao, X. Li, L. X. Yuan, X. L. Hu, W. X. Zhang, Y. H. Huang, *Adv. Mater.* **2012**, *24*, 2047.

[2] Y. M. Sun, N. A. Liu, Y. Cui, *Nature Energy* **2016**, *1*, 16071.

[3] a) S. T. Wang, Y. Yang, W. Quan, Y. Hong, Z. T. Zhang, Z. L. Tang, J. Li, *Nano Energy* **2017**, *32*, 294; b) P. C. Liu, K. J. Zhu, Y. F. Gao, H. J. Luo, L. Lu, *Adv. Energy Mater.* **2017**, *7*, 1700547; c) Y. Yue, H. Liang, *Adv. Energy Mater.* **2017**, *7*, 1602545.

[4] M. Avrami, *J. Chem. Phys.* **1941**, *9*, 177.

[5] a) Y. K. Sun, Z. H. Chen, H. J. Noh, D. J. Lee, H. G. Jung, Y. Ren, S. Wang, C. S. Yoon, S. T. Myung, K. Amine, *Nature Mater.* **2012**, *11*, 942; b) H. J. Noh, S. Youn, C. S. Yoon, Y. K. Sun, *J. Power Sources* **2013**, *233*, 121.

[6] H. Liu, Y. Y. Liu, L. W. An, X. X. Zhao, L. Wang, G. C. Liang, *J. Electrochem. Soc.* **2017**, *164*, A3666.

[7] a) S. D. Stookey, *Ind. Eng. Chem.* **1959**, *51*, 805; b) H. Shintani, H. Tanaka, *Nature Phys.* **2006**, *2*, 200.

[8] K. Lucke, K. Detert, *Acta Metall.* **1957**, *5*, 628.

[9] J. Ewing, D. Beruto, A. W. Searcy, *J. Am. Ceram. Soc.* **1979**, *62*, 580.

[10] A. Rosenflanz, M. Frey, B. Endres, T. Anderson, E. Richards, C. Schardt, *Nature* **2004**, *430*, 761.

[11] a) Y. Wang, G. Z. Cao, *Chem. Mater.* **2006**, *18*, 2787; b) N. A. Chernova, M. Roppolo, A. C. Dillon, M. S. Whittingham, *J. Mater. Chem.* **2009**, *19*, 2526; c) C. Z. Wu, F. Feng, Y. Xie, *Chem. Soc. Rev*. **2013**, *42*, 5157; d) M. Liu, B. Su, Y. Tang, X. Jiang, A. Yu, *Adv. Energy Mater.* **2017**, *7*, 1700885.

[12] a) A. Moretti, S. Passerini, *Adv. Energy Mater.* **2016**, *6*, 1600868; b) J. H. Yao, Y. W. Li, R. C. Massé, E. Uchaker, G. Z. Cao, *Energy Storage Mater.* **2018**, *11*, 205; c) G. S. Gautam, P. Canepa, W. D. Richards, R. Malik, G. Ceder, *Nano Lett.* **2016**, *16*, 2426.

[13] a) Q. L. Wei, Z. Y. Jiang, S. S. Tan, Q. D. Li, L. Huang, M. Y. Yan, L. Zhou, Q. Y. An, L. Q. Mai, *ACS Appl. Mater. Interfaces* **2015**, *7*, 18211; b) L. Q. Mai, L. Xu, C. H. Han, X. Xu, Y. Z. Luo, S. Y. Zhao, Y. L. Zhao, *Nano Lett.* **2010**, *10*, 4750; c) Z. Y. Cao, B. Q. Wei, *Nano Energy* **2013**, *2*, 481; d) Q. Liu, Z. F. Li, Y. Liu, H. Zhang, Y. Ren, C. J. Sun, W. Lu, Y. Zhou, L. Stanciu, E. A. Stach, J. Xie, *Nature Commun.* **2015**, *6*, 6127; e) C. J. Niu, M. Huang, P. Y. Wang, J. S. Meng, X. Liu, X. P. Wang, K. N. Zhao, Y. Yu, Y. Z. Wu, C. Lin, L. Q. Mai, *Nano Res.* **2015**, *9*, 128.

[14] a) H. L. Wang, X. X. Bi, Y. Bai, C. Wu, S. C. Gu, S. Chen, F. Wu, K. Amine, J. Lu, *Adv. Energy Mater.* **2017**, *7*, 1602720; b) J. W. Lai, H. H. Zhu, X. P. Zhu, H. Koritala, Y. Wang, *ACS Appl. Energy Mater.* **2019**, *2*, 1988; c) V. Petkov, P. N. Trikalitis, E. S. Bozin, S. J. L. Billinge, T. Vogt, M. G. Kanatzidis, *J. Am. Chem. Soc.* **2002**, *124*, 10157; d) Q. L. Wei, J. Liu, W. Feng, J. Z. Sheng, X. C. Tian, L. He, Q. Y. An, L. Q. Mai, *J. Mater. Chem. A* **2015**, *3*, 8070; e) S. Tepavcevic, J. G. Connell, P. P. Lopes, M. Bachhav, B. Key, C. Valero-Vidal, E. J. Crumlin, V. R. Stamenkovic, N. M. Markovic, *Nano Energy* **2018**, *53*, 449.

[15] a) L. Q. Mai, C. S. Lao, B. Hu, J. Zhou, Y. Y. Qi, W. Chen, E. D. Gu, Z. L. Wang, *J. Phys. Chem. B* **2006**, *110*, 18138; b) J. Z. Sheng, Q. D. Li, Q. L. Wei, P. F. Zhang, Q. Q. Wang, F. Lv, Q. Y. An, W. Chen, L. Q. Mai, *Nano Res.* **2014**, *7*, 1604.

[16] S. T. Wang, W. Quan, Z. Zhu, Y. Yang, Q. Liu, Y. Ren, X. Y. Zhang, R. Xu, Y. Hong, Z. T. Zhang, K. Amine, Z. L. Tang, J. Lu, J. Li, *Nature Commun.* **2017**, *8*, 627.

[17] a) S. Sarkar, P. S. Veluri, S. Mitra, *Electrochim. Acta* **2014**, *132*, 448; b) Y. Xu, H. S. Dong, M. Zhou, C. L. Zhang, Y. H. Wu, W. Li, Y. L. Dong, Y. Lei, *Small Methods* **2019**, *3*, 1800349.

[18] a) H. A. Abbood, H. Peng, X. H. Gao, B. E. Tan, K. X. Huang, *Chem. Eng. J.* **2012**, *209*, 245; b) L. J. Mao, C. Y. Liu, J. Li, *J. Mater. Chem.* **2008**, *18*, 1640.

[19] a) T. N. Vo, H. Kim, J. Hur, W. Choi, I. T. Kim, *J. Mater. Chem. A* **2018**, *6*, 22645; b) Y. Y. Liu, M. Clark, Q. F. Zhang, D. M. Yu, D. W. Liu, J. Liu, G. Z. Cao, *Adv. Energy Mater.* **2011**, *1*, 194.

[20] a) H. Yamada, K. Tagawa, M. Komatsu, I. Moriguchi, T. Kudo, *J. Phys. Chem. C* **2007**, *111*, 8397; b) A. Q. Pan, H. B. Wu, L. Zhang, X. W. Lou, *Energy Environ. Sci.* **2013**, *6*, 1476.

[21] a) Y. S. Cai, J. Zhou, G. Z. Fang, G. M. Cai, A. Q. Pan, S. Q. Liang, *J. Power Sources* **2016**, *328*, 241; b) K. W. Yang, G. Z. Fang, J. Zhou, M. L. Qin, Y. Tang, A. Q. Pan, S. Q. Liang, *J. Power Sources* **2016**, *325*, 383; c) Y. Sun, S.-B. Yang, L.-P. Lv, I. Lieberwirth, L.-C. Zhang, C.-X. Ding, C.-H. Chen, *J. Power Sources* **2013**, *241*, 168; d) P. F. Zhang, L. Z. Zhao, Q. Y. An, Q. L. Wei, L. Zhou, X. J. Wei, J. Z. Sheng, L. Q. Mai, *Small* **2016**, *12*, 1082; e) C. F. Zhang, Z. X. Chen, Z. P. Guo, X. W. Lou, *Energy Environ. Sci.* **2013**, *6*, 974; f) J. Yan, A. Sumboja, E. Khoo, P. S. Lee, *Adv. Mater.* **2011**, *23*, 746; g) C. H. Han, M. Y. Yan, L. Q. Mai, X. C. Tian, L. Xu, X. Xu, Q. Y. An, Y. L. Zhao, X. Y. Ma, J. L. Xie, *Nano Energy* **2013**, *2*, 916; h) Y. P. Wang, Z. W. Nie, A. Q. Pan, Y. F. Zhang, X. Z. Kong, T. Zhu, S. Q. Liang, G. Z. Cao, *J. Mater. Chem. A* **2018**, *6*, 6792; i) L. Q. Mai, Q. Y. An, Q. L. Wei, J. Y. Fei, P. F. Zhang, X. Xu, Y. L. Zhao, M. Y. Yan, W. Wen, L. Xu, *Small* **2014**, *10*, 3032; j) Y. W. Li, J. H. Yao, E. Uchaker, J. W. Yang, Y. X. Huang, M. Zhang, G. Z. Cao, *Adv. Energy Mater.* **2013**, *3*, 1171; k) D. B. Kong, X. L. Li, Y. B. Zhang, X. Hai, B. Wang, X. Y. Qiu, Q. Song, Q. H. Yang, L. J. Zhi, *Energy Environ. Sci.* **2016**, *9*, 906; l) Q. L. Wei, S. S. Tan, X. Y. Liu, M. Y. Yan, F. C. Wang, Q. D. Li, Q. Y. An, R. M. Sun, K. N. Zhao, H. Wu, L. Q. Mai, *Adv.*

Funct. Mater. **2015**, *25*, 1773; m) Y. H. Dai, Q. D. Li, S. S. Tan, Q. L. Wei, Y. X. Pan, X. C. Tian, K. N. Zhao, X. Xu, Q. Y. An, L. Q. Mai, Q. J. Zhang, *Nano Energy* **2017**, *40*, 73; n) H. Y. Wang, K. L. Huang, C. H. Huang, S. Q. Liu, Y. Ren, X. B. Huang, *J. Power Sources* **2011**, *196*, 5645.

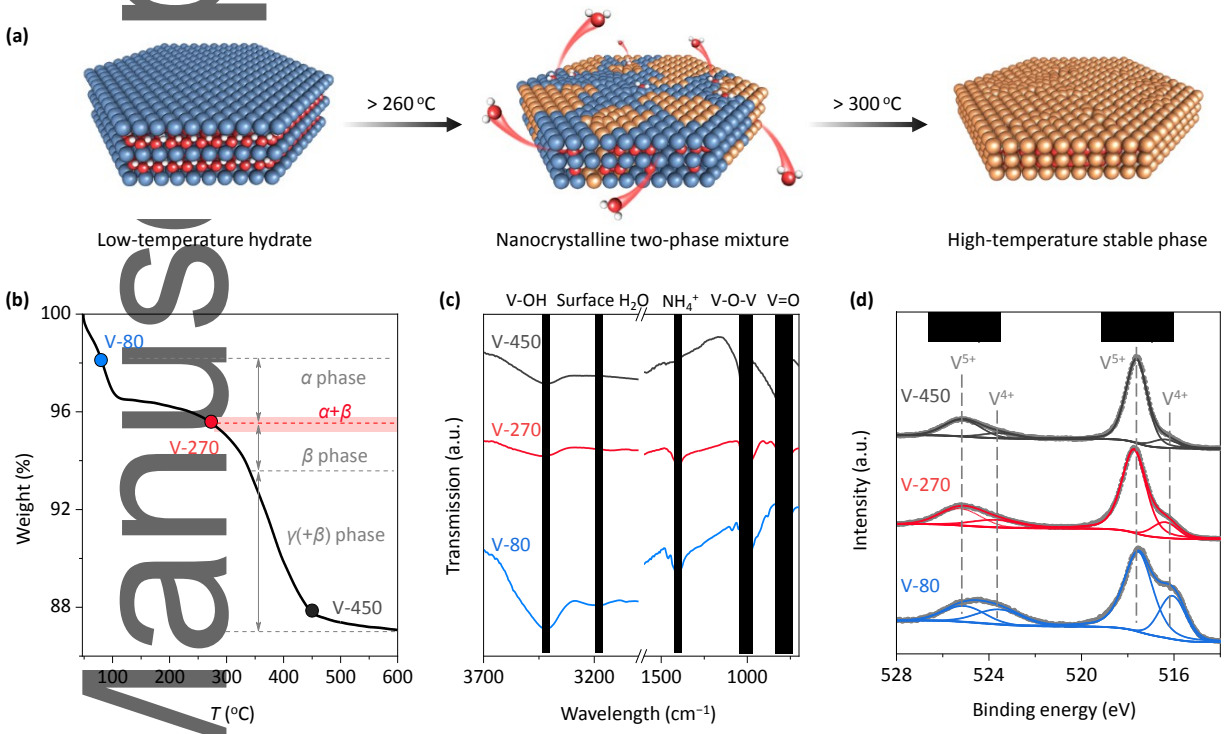

Figure 1. (a) Schematic reaction mechanism during heat treatment. (b) TGA analysis of V-P precursor. (c) FTIR and (d) XPS of samples heat-treated at 80 °C, 270 °C and 450 °C.

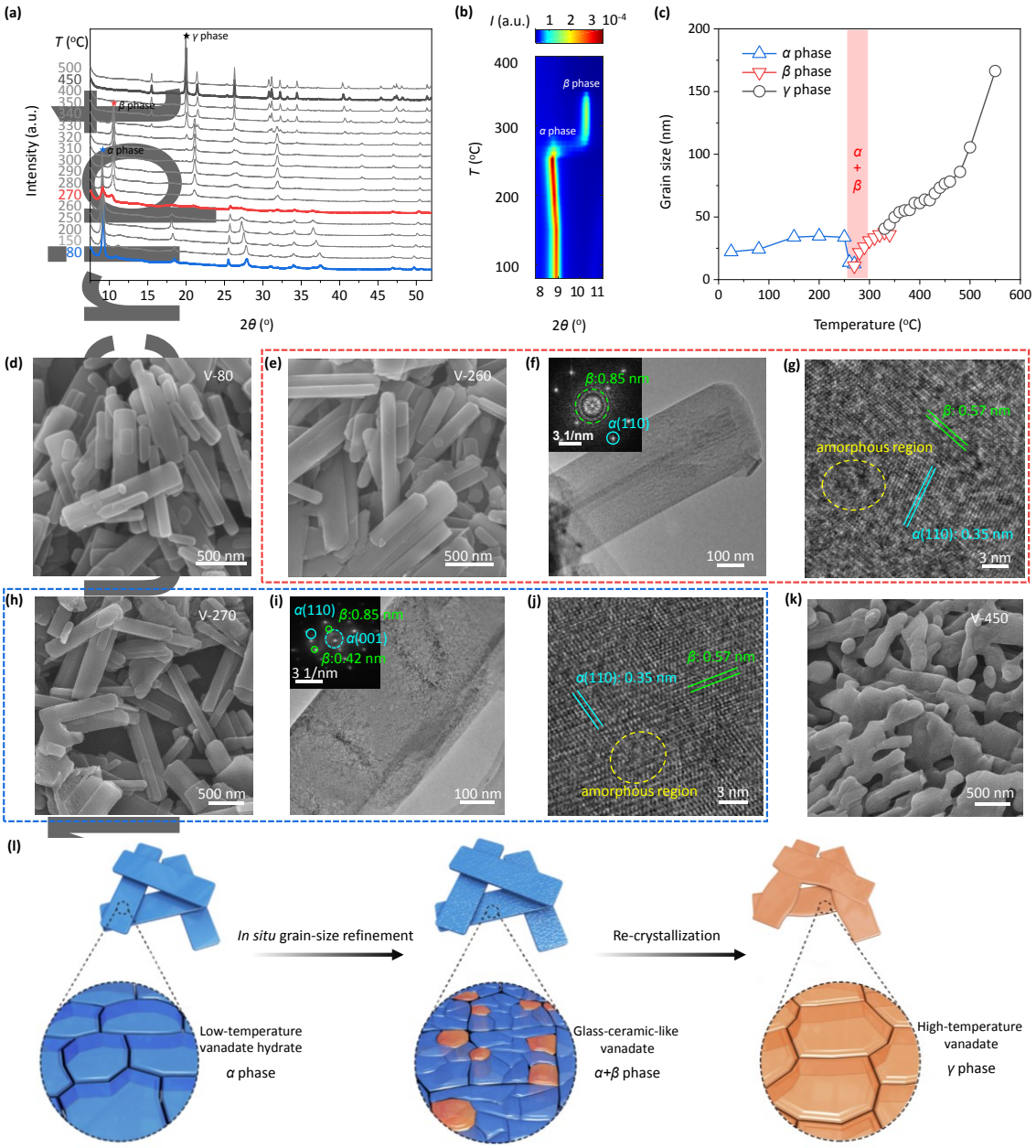

Figure 2. (a) *In situ* XRD patterns and (b) contour plot of magnified low-angle regions (2ϑ=8-11°) upon heating. (c) Calculated grain size from (a). (d) SEM image of V-80. (e) SEM, (f) TEM and (g) HRTEM images of V-260. Inset of (f): selected area diffraction. (h) SEM, (i) TEM and (j) HRTEM images of V-270. Inset of (i): selected area diffraction. (k) SEM image of V-450. (l) Schematic phase transition process with varying grain sizes.

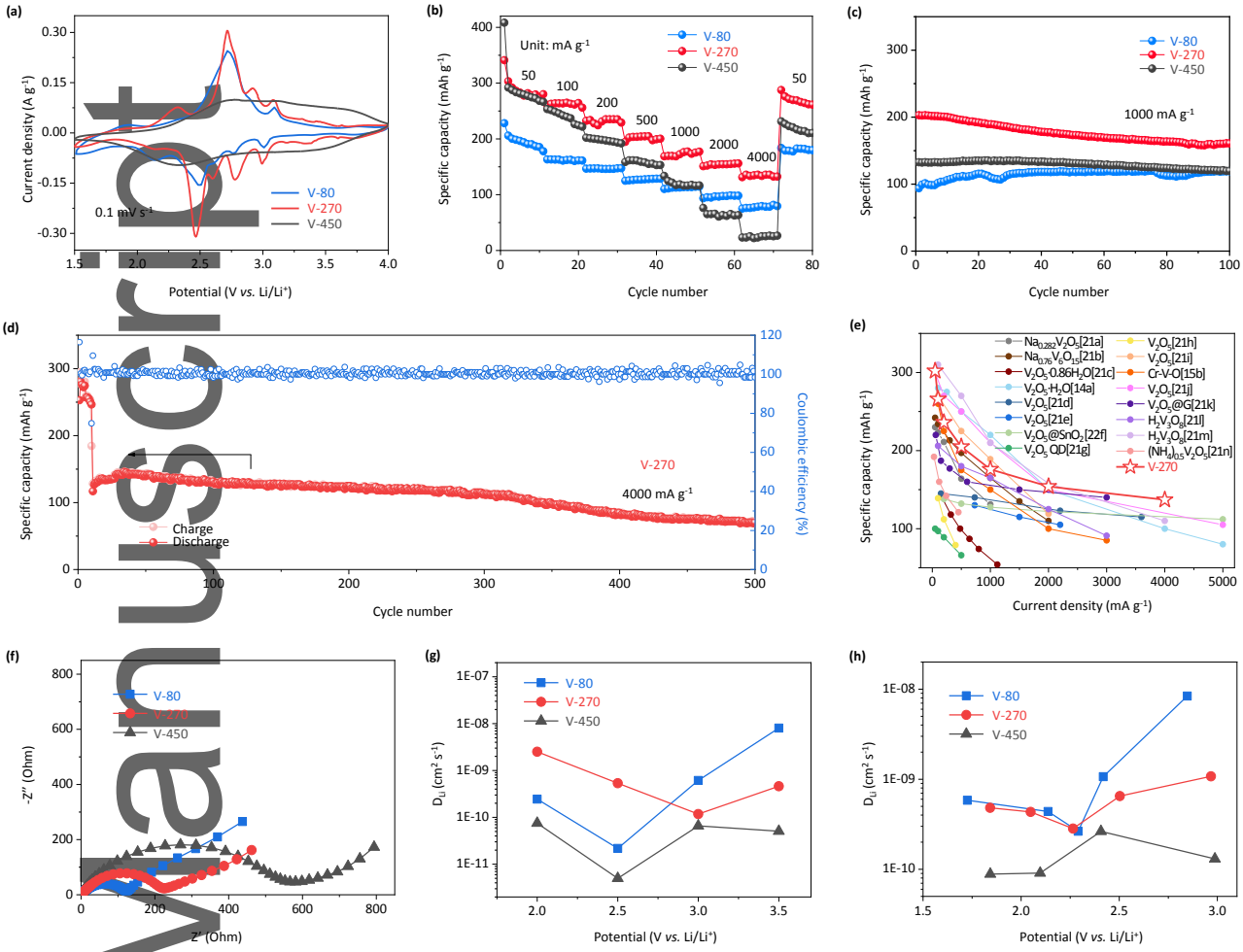

Figure 3. (a) CV curves, (b) rate performance and (c) cycling performance at 1000 mA g^{-1} of V-80, V-270 and V-450. (d) Cycling performance of V-270 at 4000 mA g^{-1}. (e) Comparison for rate performance of V-270 with literature data in vanadate related systems. (f) EIS results of fully charged V-80, V-270 and V-450 after 5 cycles. Lithium ion diffusivity calculated from (g) EIS and (h) GITT data at different voltages.

Glass-ceramic-like vanadate cathodes can be easily obtained by a fine tuning of heat treatment process, offering abundant internal boundaries that facilitate lithium ion diffusion and minimize side reactions.

Glass-ceramic-like vanadate cathodes for high-rate lithium-ion batteries

Keywords: Microstructures, kinetics, batteries, cathodes, vanadate

TOC figure